Ultra-compact Camera Pixel with Integrated Plasmonic Color Filters

Evgeniy Panchenko*[1,2], Lukas Wesemann[1], Daniel E. Gómez[2,3], Timothy D. James[1], Timothy J. Davis[1], and Ann Roberts[1]

[1]*School of Physics, University of Melbourne, Victoria 3010, Australia*

[2]*Melbourne Centre for Nanofabrication, Australian National Fabrication Facility, Clayton, Victoria 3168, Australia*

[3]*RMIT University, Victoria 3000, Australia*

Abstract

Photodetector size imposes a fundamental limit on the amount of information that can be recorded by an image sensor. Compact, high-resolution sensors are generally preferred for portable electronic devices such as mobile phones and digital cameras, and as a result, a significant effort has been invested in improving the image quality provided by small-area image sensors. Reducing photodetector size, however, still faces challenges in implementation requiring improvements in current technology to meet the demand for ultra-compact imaging systems such as cameras. An issue with a decrease in size is associated with photodetectors utilizing color filters. In most commonly used camera designs these filters are made of dyes or pigments and incompatible with the CMOS fabrication process. They are, therefore, fabricated in two different technological processes and require subsequent alignment. As the pixel size decreases, the alignment of these layers becomes

---

*evgeniy.panchenko@unimelb.edu.au

challenging. Furthermore, dye-based filters need to have a thickness of the order of micrometers to ensure sufficient absorption. Here we propose and experimentally demonstrate a compact, low-cost color sensor utilizing monolithically integrated plasmonic antennas that have a nanoscale thickness and are fabricated in the same technological process with photodetector matrix.

Since its invention, the digital camera has become ubiquitous in modern electronic devices such as laptops and smartphones. The utilization of optical sensors is not limited to the consumer segment but is central to scientific [1, 2] and biomedical applications such as point-of-care devices and endoscopy where cameras with high resolution, speed and sensitivity are important. Cameras with an extended wavelength sensitivity into the ultraviolet, near-IR and deep infrared regions of the spectrum [3, 4] are also becoming more widely used.

The pixel is an elementary unit of the digital camera and its size imposes a fundamental constraint on the amount of information that can be recorded on a sensor with a certain area. Since compact, high-resolution sensors are of greatest interest for portable devices such as mobile phones and digital cameras, a significant effort has been made in improving the image quality provided by small-area sensors [5, 6]. Various technological approaches such as deep trench isolation [7] and back side illumination [8] were proposed to reduce the pixel size below 1.2 µm. Although there has been remarkable success in recent years [9], reducing the pixel size still faces challenges in implementation and requires improvements in current technology to meet the demand for ultra-compact image sensors.

The operating principle of the majority of commercially available color camera sensors is based on the design shown in Figure 1a. The incoming light passes through a mosaic filter with a particular color pattern. The color filters usually incorporate dyes or pigments and transmit a particular wavelength spectrum while the remainder is absorbed [10]. These filters provide wavelength selectivity since the sensor itself has a broad wavelength response. The filtered light is then incident on an array of photodetectors. Each cell represents a single pixel and is dedicated to sensing a certain part of the visible spectrum

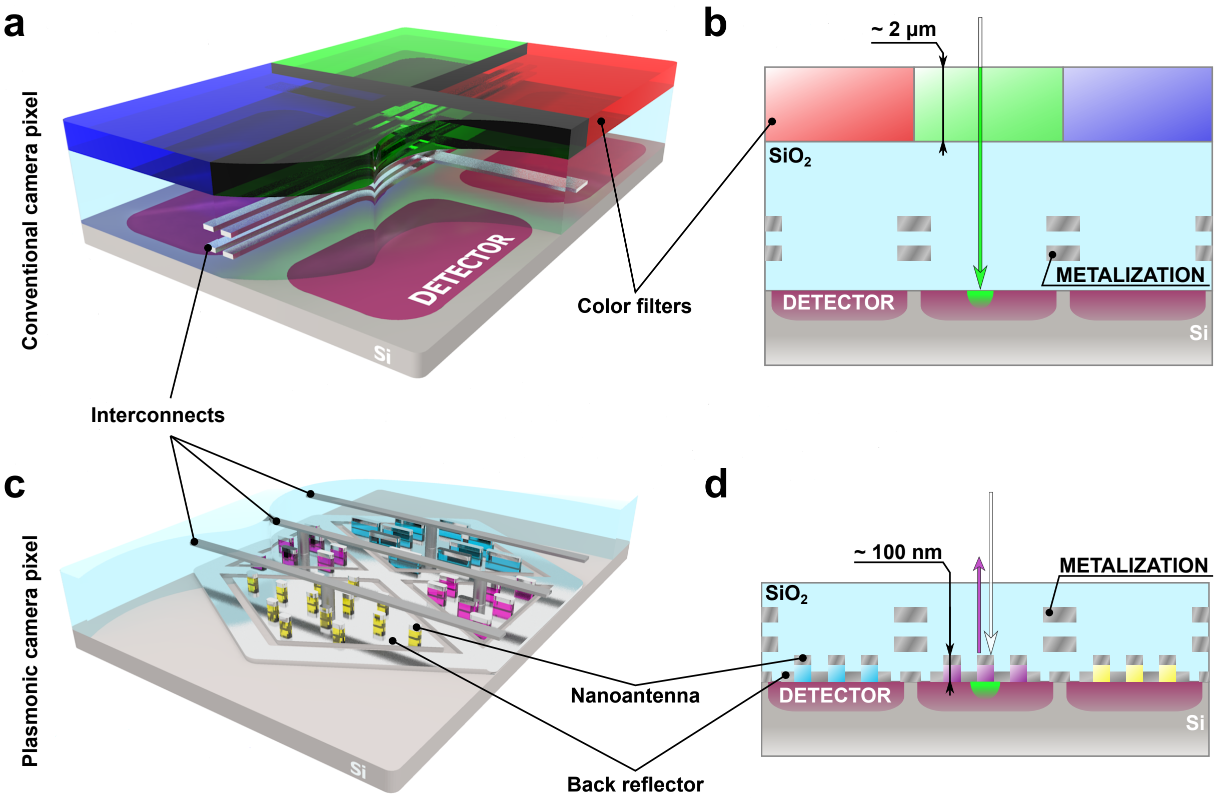

Figure 1: Schematic representation of conventional **(a)** and plasmonic **(c)** color photodetectors. Figures **(b,d)** show the corresponding cross sections of color sensors.

in one region of the image. Figure 1b shows a schematic representation of cross-sections through three pixels each responsible for detection of either red, green or blue regions of the visible spectrum. The filters and the photodetector integrated circuit are fabricated separately and subsequently combined in a separate step. As the pixel size decreases, the alignment of these layers becomes challenging. Moreover, the requirement for two different fabrication processes as well as additional alignment steps increases the final cost of the camera matrix.

In contrast, filters based on the phenomenon of localized surface plasmons (LSPs) provide an opportunity to decrease the pixel size to micrometer or even sub-micrometer dimensions [11, 12]. It was shown recently [13, 14, 15] that plasmonic nanoantenna structures based on the principals of a perfect absorber [16, 17] can be used to create CMY color filters. The technique permits the fabrication of plasmonic pixels which are capable of producing a wide color gamut [13, 18, 19]. color filters based on LSP resonances require no dyes or pigments and are fully compatible with CMOS fabrication process. These filters were designed to operate in reflection mode and have been shown to be robust to off-normal angles of incidence [13, 16] and exhibit a strong polarization response. Furthermore, these filters have a thickness below 100 nm compared to conventional color filters that are an order of magnitude thicker.

Here we propose and experimentally demonstrate a compact, low-cost color sensor incorporating monolithically integrated nanoscale thickness plasmonic antennas that are fabricated in the same technological process with photodetector matrix. Although color transmission filters have been introduced onto monochrome pixelated sensors to permit color sensitivity [11, 20], there have been few reports of monolithic integration of filters into silicon sensors. One of the biggest challenges is associated with a high refractive index of silicon as it is known to have a significant effect on the wavelength of plasmonic resonances and this must be incorporated into the design of the filter.

A schematic representation of this sensor and its cross-section are shown in Figures 1c and 1d respectively. The plasmonic antenna arrays responsible for spectral filtering are embedded into the pixel channels. The color filters, therefore, are located on the surface of the detectors. The monolithic, single step fabrication of sensor and color filter eliminates the necessity of filter alignment with the underlying sensors. Along with the reduced set of materials required, this potentially significantly reduces the cost of fabrication and, in turn, the final cost of a product. The polarization sensitivity of these devices is also important in applications involving imaging through smoke or fog or to minimize reflection glare. Finally, the combination of proximity of the filter to the detector and its extremely small thickness of 130 nm results in potential reduction of the optical cross-talk [21, 22].

The sensors demonstrated here were chosen to have a hexagonal shape and a total size of 20 µm, but could have smaller dimensions (of the order of 1 µm) as long as it accommodates several periods of the nanoantenna array (see **Supplementary Materials** section for demonstration of a 2 µm pixel array). Each sensor consists of three Schottky photodetectors with plasmonic color filters (see Fig.2a,d). These filters are designed to

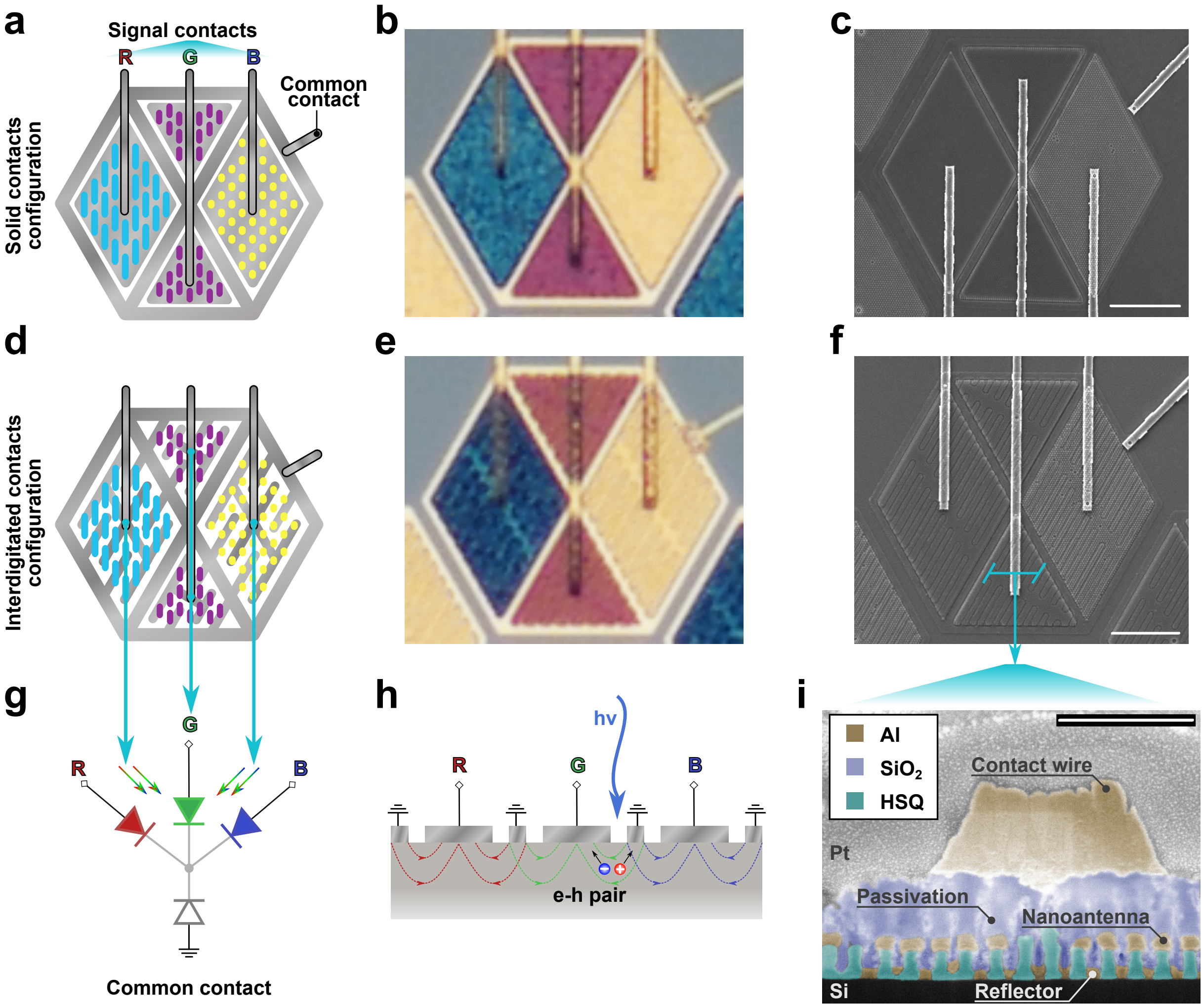

Figure 2: Schematic diagrams of plasmonic color sensor with solid **(a)** and interdigitated **(d)** contact configurations. Figures **(b,e)** and **(c,f)** show the corresponding optical and SEM images respectively. The equivalent electric circuit of the plasmonic color sensor **(g)** is represented by 4 Schottky diodes with common cathode. Schematic cross section of the color sensor is shown in **(h)**. SEM image of magenta photodetector channel cross section taken at 52^o tilt is shown in figure **(i)**. The scale bar for images **(c,f)** is 5 µm and 300 nm for image **(i)**.

reflect the region of the spectrum associated with cyan, magenta and yellow colors (see Fig.2b,e). The back-reflector of each plasmonic filter serves as an anode contact for the photodiode. Here we demonstrate two possible contact configurations: solid (see Fig.2a,b,c) and interdigitated (see Fig.2d,e,f). The common contact surrounds the color channels and also forms a Schottky barrier with a substrate. The equivalent electric circuit is represented by four Schottky diodes with connected cathodes (see Fig.2g). Each color channel is, therefore, a metal-semiconductor-metal (MSM) photodiode integrated with a plasmonic color filter [23, 24, 25]. When a bias is applied, an electric field gradient is formed between the common electrode and the back-reflector of each plasmonic filter forming three active photodetector regions (see Fig.2h). The common electrode splits the channels and also acts as a screen. The electron-hole pairs generated in one pixel channel will not be able to reach the neighboring channels as there is no electric field gradient between them. When the corresponding wavelength is reflected by the filter, the transmitted light will be absorbed in the active region of the detector resulting in photocurrent generation. The sensor channels are, therefore, responsible for detecting the red, green and blue parts of the spectrum respectively. A scanning electron microscope (SEM) cross-section of a magenta photodetector channel is shown in Figure 2i.

The principle underlying plasmonic perfect absorbers is based on the coupling between the plasmonic resonance of the nanoantenna and Fabry-Perot resonances of the gap between antenna and substrate. Figure 3a shows a schematic representation of a perfect absorber structure consisting of a nanoaperture in a metal film with a nanoantenna suspended above the surface. The enhancement effect is maximal when the distance between nanoantenna and an reflecting film is $(2m + 1)\lambda/4$ where m is an integer and λ is a wavelength in the coating [13]. The overlap between the plasmonic and Fabry-Perot resonances increases the strength of the plasmonic response significantly. The perfect absorber configuration, therefore, permits sharper resonances compared to common nanoantenna arrays.

In the plasmonic color sensor presented here, hydrogen silsesquioxane (HSQ) pillars with a height of 90 nm are used to support the aluminum nanoantennas above the aluminum back-reflector. The thickness of the HSQ was chosen to locate the peak of perfect absorber resonance at 532 nm. The antennas were arranged in a hexagonal lattice. The entire structure was covered with a 180 nm thick passivation layer of SiO_2 (see **Fabrication** section for more details). Since the dielectric permittivities of HSQ and SiO_2 are very similar, the nanoantennas are, in fact, embedded into what is optically an effectively homogeneous medium.

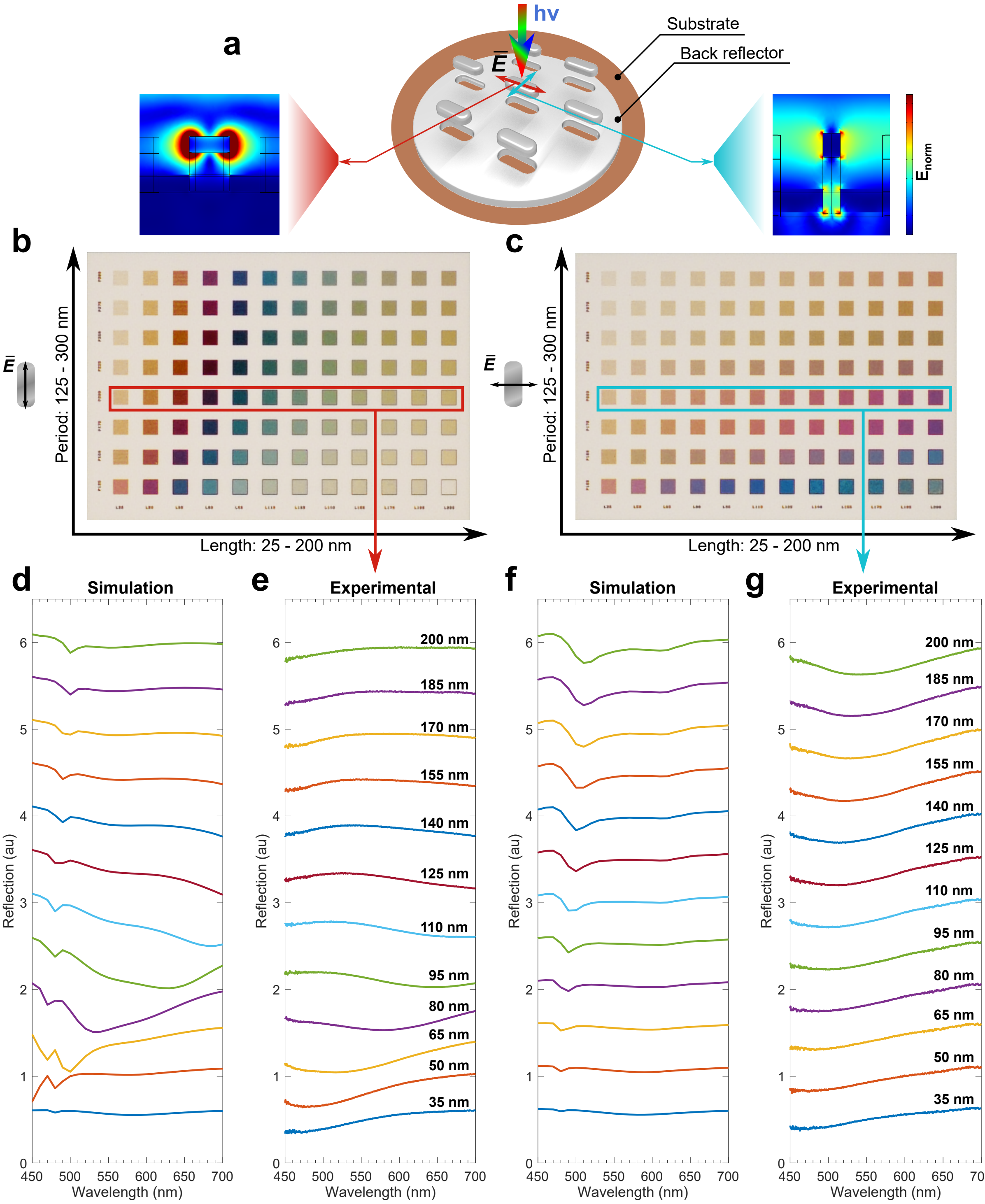

Figure 3: Schematic representation of a perfect absorber structure **(a)**. Optical images of plasmonic color filters with different lattice period and nanoantenna length under y- **(b)** and x- **(c)** polarized illumination. Figures **(d,e)** and **(f,g)** show corresponding simulation and experimental data sets for filters with a fixed period of p = 200 nm and various lengths.

Having the distance between the nanoantennas and the back-reflector fixed, the resonance of the array is, therefore, defined by the period, length of the nanoantenna and polarization of the incident wave. Figures 3b and 3c show the bright field images of plasmonic color filters with 125 - 300 nm lattice periods and 25 - 200 nm long nanoantennas under y- and x-polarized illumination respectively. Several phenomena such as localized surface plasmon resonances of nanoantenna and nanoapertures, effects associated with periodic array diffraction and mode coupling between the nanoantenna and metal film all contribute to the spectra giving a vast parameter space for optimization.

Simulations of the reflection spectra from the antenna arrays (see Fig.3d,f) performed using the Finite Element Method (FEM) are in a good agreement with the experimental data (see Fig.3e,g). The resonant features around 480 nm in the simulated reflection spectra are Wood's anomalies [26]. The features do not appear in the experimental results due to the angle-averaging effect of the high numerical aperture objective used (see **Characterization** section for more details). These simulations were used to determine optimal parameters for the nanoantennas for each of the color filters. As can be seen from the reflection spectra, both polarizations produce vivid colors. On the other hand, the maximum transmission through the filter is achieved when the electric field is perpendicular to the nanoantennas (i.e the magnetic field is parallel to the nanoapertures underneath). This polarization was, therefore, used to produce the plasmonic color filters. In the design of the sensors presented here, the nanoantenna arrays with antenna lengths of 170, 200, 35 nm and array periods of 125, 150, 175 nm were used for the cyan, magenta and yellow color filters respectively. These combinations provide the most saturated colors, resulting in a high channel selectivity.

Current-voltage (IV) characteristics of sensors with solid and interdigitated contacts are shown in Figures 4a and 4c respectively. The shape of the curves is typical for MSM photodetectors [24]. The asymmetry of the curves under positive and negative bias can be explained by the different areas of the common contact and the back-reflectors of the color channels. An IV curve of the magenta channel with a solid back-reflector contact

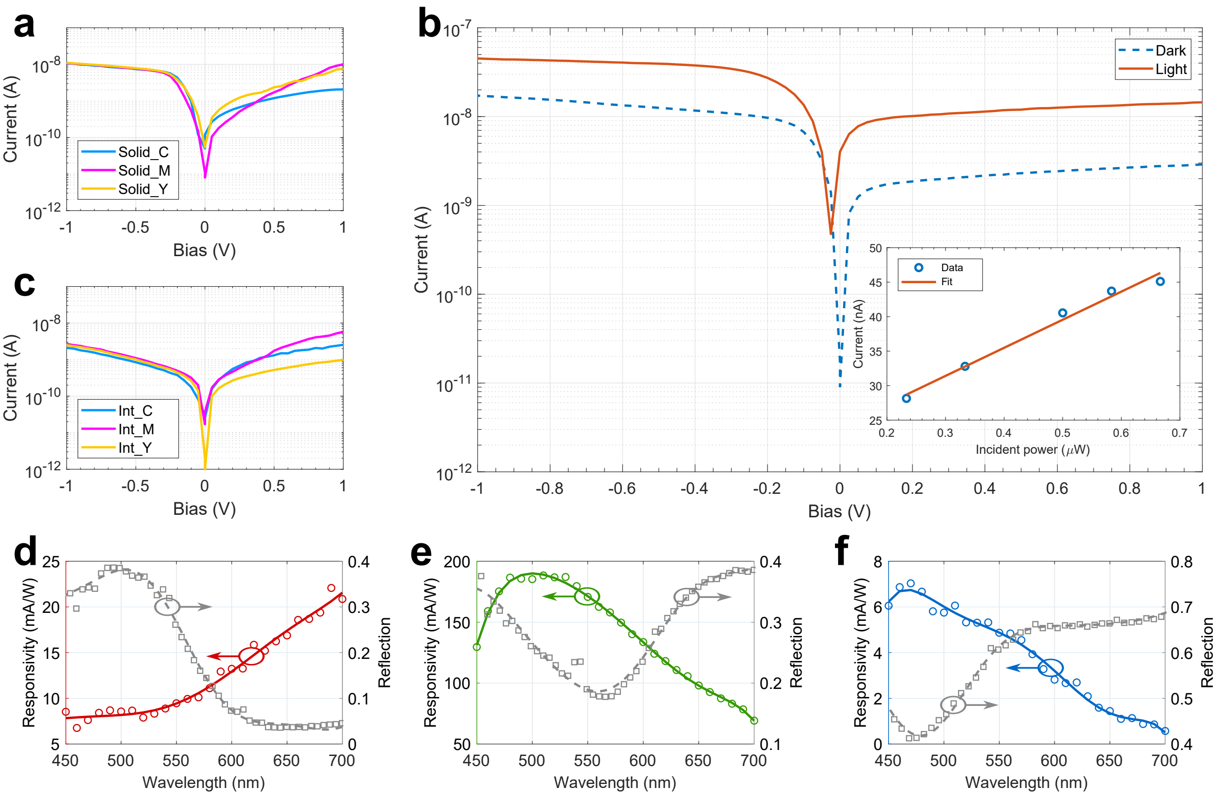

Figure 4: Current voltage (IV) characteristics of each channel of the plasmonic color sensor utilizing solid **(a)** and interdigitated **(c)** electrode configurations respectively (with no illumination). IV characteristics of magenta channel **(b)** without (dashed line) and with (solid line) 0.66 µW illumination (635 nm wavelength). The inset shows generated photocurrent as a function of an incident power (direct illumination, -1 V bias, 635 nm wavelength). Responsivity curves of cyan **(d)**, magenta **(e)** and yellow **(f)** channels with interdigitated electrodes configuration. The gray lines show the corresponding normalized reflection from these channels.

under illumination is shown in Figure 4b. The inset shows the photocurrent generated by the photodetector as a function of the incident laser power at 635 nm wavelength and -1 V bias. The straight line fit demonstrates the linear response of the photodetector.

The responsivity curves of the cyan, magenta and yellow channels of the sensor with the interdigitated contact configuration as a function of incident wavelength are shown in Figures 4d,4e and 4f respectively. The measurements were obtained from various sensors across the same sample. During the experiment, the power at each wavelength was fixed at around 1 µW (see **Characterization** section for more details). As can be seen, the channels appearing in Figures 4d,e,f as cyan, magenta and yellow have a maximum responsivity in the red, green and blue parts of the spectrum respectively. The photoresponse of the sub-channels is in a good agreement with what would be expected from the reflection spectra collected from the corresponding plasmonic filters (dashed curves). It should be noted that since in MSM photodiodes the detection occurs in a thin layer close to the surface where the largest field gradient is observed [25, 27] the responsivity at shorter wavelengths is slightly enhanced. This produces a small blue-shift of the magenta channel responsivity. The lower responsivity of the cyan and yellow channels compared to the magenta may be explained by contamination at the metal-semiconductor interface as Schottky barrier-based devices are extremely sensitive to surface quality [27, 28]. The responsivity, therefore, can be further enhanced by improving the Schottky barrier quality for example by introducing a thin oxide layer between Si substrate and a metal contact [29].

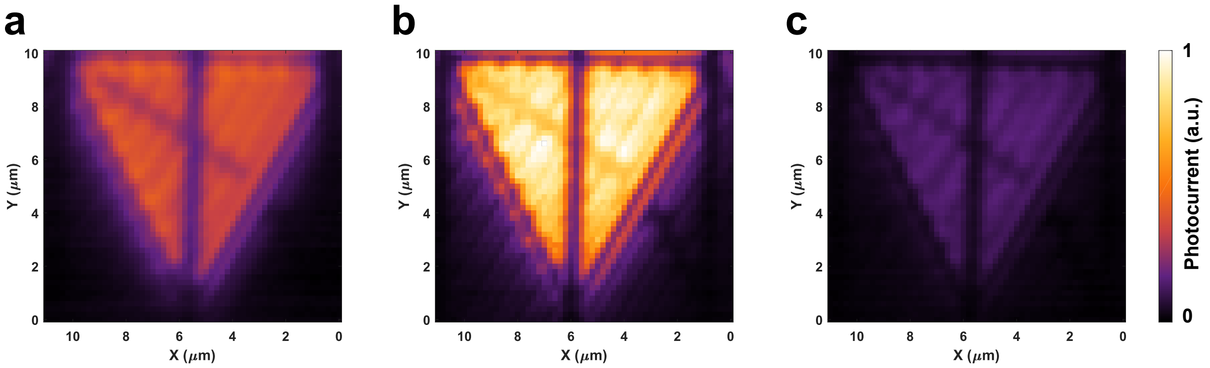

Figure 5: Normalized SPCM images of magenta channel of plasmonic color sensor with interdigitated electrode configuration collected at 450 nm **(a)**, 532 nm **(b)** and 650 nm **(c)** wavelengths respectively. The power at each wavelength was 0.5 µW.

The photodetectors were further characterized using scanning photocurrent microscopy (SPCM) [30] (see **Characterization** section for more details). The magenta channel of the plasmonic color sensor was scanned with a highly focused, polarized beam at wavelengths of 450, 532 and 650 nm with 10 nm FWHM bandwidth. During the experiment the power at each wavelength was held constant at 0.5 µW. The dark current was subtracted and the images were normalized to the maximum photocurrent value generated at a wavelength of 532 nm. The resulting normalized SPCM images are shown in Figures 5a, 5b and 5c respectively. As expected, the maximum photocurrent is generated when the magenta channel is illuminated with green light. It can also be seen that the channel generates more photocurrent at 450 nm compared to 650 nm wavelength. This is due to the slight blue-shift of the responsivity peak and confirms the photoresponse for this channel shown in Figure 4e.

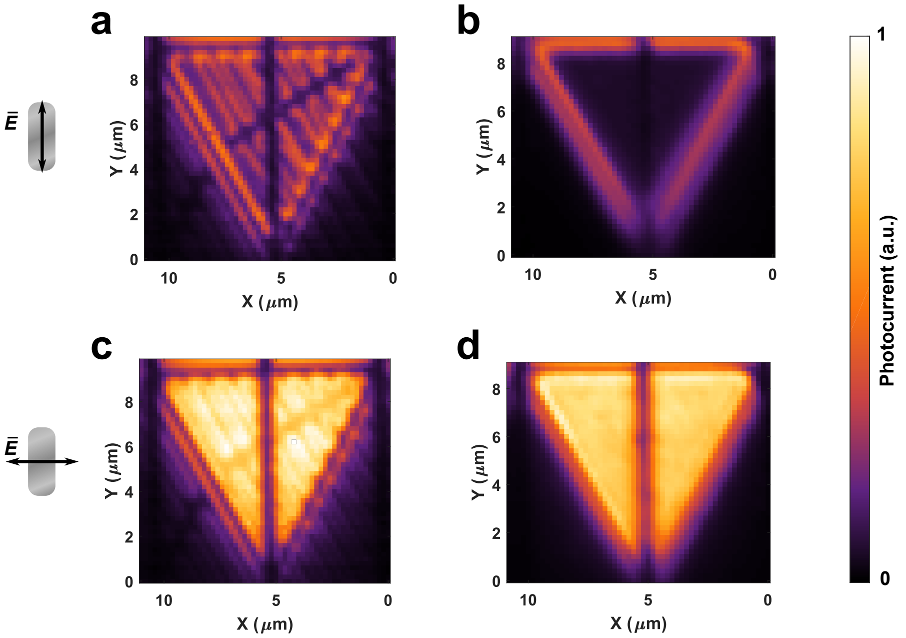

Figure 6: Normalized SPCM images of magenta channels of plasmonic color sensors with interdigitated **(a,c)** and solid **(b,d)** electrode configurations collected at orthogonal polarization states. The images were collected at 532 nm wavelength.

The polarization selectivity of both plasmonic color sensor designs was also studied using SPCM. This also provides validation of the physical mechanisms underpinning the device performance. The magenta channels of both sensors were scanned using orthogonally polarized beams at 532 nm. Normalized SPCM images of the magenta channels scanned with y-polarized light are shown in Figures 6a,b. The dark regions on the filters imply that a large portion of power has been reflected by the filter, resulting in fewer electron-hole pairs generated in the semiconductor. On the other hand, the largest generated photocurrent for both sensor configurations was observed when the electric field of the incident light is directed perpendicular to the nanoantennas (see Fig.6c,d). This polarization state corresponds to the maximum transmission through the plasmonic color filter.

The utilization of plasmonic metasurfaces as color filters instead of conventional pigments permits planarization of the pixel design and avoids necessity of additional alignment steps. It also enables scaling down the overall dimensions of the sensor to below 1 µm. Both photodetector configurations shown here demonstrated an ability to distinguish between different spectral bands. It is more likely that the solid contact configuration will be better as the size of the photodetector decreases since it will provide a larger contact area and, therefore, may exhibit better responsivity. Furthermore, the photodetectors exhibited an intrinsic polarization sensitivity which is important for applications including those involving imaging through scattering media. Although the pixels shown were designed for the visible part of the electromagnetic spectrum it is possible to extend the sensitivity range into the UV and near-IR regions, creating a 'hyperspectral' pixel configurations with more than three channels. color sensors with embedded plasmonic metasurfaces, therefore, can be used as a planar nanoscale alternative to conventional color pixels in future high-resolution consumer or scientific cameras.

1 Acknowledgments

This research was supported under the Australian Research Council's Discovery Projects funding scheme (project number DP160100983). This work was performed in part at the Melbourne Centre for Nanofabrication (MCN) in the Victorian Node of the Australian National Fabrication Facility (ANFF). D.G. acknowledges the ARC for support through a Future Fellowship (FT140100514).

2 Methods

2.1 Simulations

Finite element method (FEM) analysis, implemented in COMSOL Multiphysics 5.3 with RF module, was used to simulate the reflection spectra from plasmonic nanoantenna arrays. Periodic boundary conditions were used to obtain the spectra from an assumed infinitely large array of nanoantennas. A mesh with a maximum element size of 10 nm was used in the areas where a high simulation accuracy is desired (specifically the nanoantennas and nanoapertures). The optical properties of Al used in the model were taken from experimental data for bulk material [31].

2.2 Fabrication

Photodetectors were fabricated on low doped n-type silicon wafer with a bulk resistance of ρ = 1-10 Ωcm. A sequential ultrasonic cleaning in acetone, IPA and deionized water was performed to remove any contamination that might be present on the wafer. It was then spin-coated with a 90 nm thick layer of 6% HSQ and baked for 3 min at 60^{o}C. In the first lithography step the raised pillars were exposed using a 100 kV EBPG5000+ electron beam lithography (EBL) system. The pattern was developed in NaOH:NaCl 1%:4% wt. solution for 4 min.

The sample was then spin-coated with a 280 nm thick layer of PMMA A4 950k resist and baked at 180^{o}C for 5 min. The first metallization layer was exposed using the same EBL system. The pattern was then developed in 1:3 MIBK:IPA solution for 1 minute. The aluminum layer with a thickness of 40 nm was deposited at 0.7 A/s evaporation rate using an IntlVac NanoChrome II electron-beam evaporation system. After evaporation a lift-off step in a hot acetone followed by rinsing in IPA was performed. A 180 nm thick passivation layer of SiO_2 was grown on the sample using an Oxford Instruments PLASMALAB 100 PECVD system.

The sample was then spin-coated with a 1 µm thick layer of PMMA A6 950k resist and baked at 100^{o}C for 30 min then at 180^{o}C for 15 min. The pattern defining interlayer vias was exposed using the same EBL system. The pattern was then developed in 1:3 MIBK:IPA solution for 1 minute. The developed sample was transferred into an Oxford Instruments PLASMALAB 100 ICP380 reactive ion etching tool. A combination of He and C_4F_8 gases with flow speeds of 70 and 10 sccm respectively was used to etch the

SiO_2 layer. The etching was performed at a pressure of 5 mTorr for 70 s. The remaining PMMA was removed using oxygen plasma and hot acetone bath followed by rinsing in IPA.

The sample was then spin-coated with a 1000 nm thick layer of PMMA A6 950k resist and baked at 100^{o}C for 30 min then at 180^{o}C for 15 min. The pattern defining the interconnects was exposed using same EBL system. The pattern was then developed in a 1:3 MIBK:IPA solution for 1 minute. The developed sample was transferred into an Intlvac Nanochrome AC/DC sputterer and 300 nm of Al was deposited onto the sample. After sputtering, a lift-off step in hot acetone followed by rinsing in IPA was performed.

Finally, the sample was coated with 600 nm PMMA A4 layer to protect the structures during the next step. A wet dicing saw (Disco DAD321) was used to separate the photodetectors. The samples were glued into a ceramic LCC20 package and bonded using a Kulicke & Soffa 4522D Wedge bonder with aluminum wire.

2.3 Characterization

A Fianium SC450 supercontinuum white light source was used to obtain reflectance spectra from the samples. It was coupled with a Fianium SuperChrome VIS tunable filter to obtain spectrally resolved measurements. A combination of polarizer with a half-wave plate was used to produce and control the linear polarization of the beam. The half-wave plate AHWP05M-600 was mounted in a Thorlabs PRM1Z8 rotation stage. Utilization of Nikon CFI Plan Fluor 100x 0.7 NA long working distance objective permitted the uniform illumination of the color filter area.

For photoresponsivity measurements three transimpedance amplifiers were designed and fabricated to work with the photodetector. The amplification coefficient was fixed on both channels and set to 10^6. A Keithley 487 source meter was used for precision biasing. The signal from the amplifiers was then sampled with a National Instruments USB-6343 DAQ. The whole plasmonic sensor area was illuminated using the Nikon CFI Plan Fluor 50x 0.55 NA long working distance objective. A Thorlabs PM100D optical power meter with S121C power sensor was used to monitor the power. During the measurement, the power at each wavelength was held constant at 3 µW so that each color channel receives 1/3 of the total power by adjusting the Q-factor of the Fianium white light source.

For SPCM measurements the same white light source and tunable filter were used together with the 100x long working distance objective described above to obtain a highly focused spot and to scan the device footprint. The resolution in both x and y directions was of approximately 200 nm.

References

[1] F. M. Reininger, *Imaging spectrometer/camera having convex grating* **2000**, US Patent 6,100,974.

[2] J. Itatani, F. Quéré, G. L. Yudin, M. Y. Ivanov, F. Krausz, P. B. Corkum, *Phys. Rev. Lett.* **2002**, *88*, 173903.

[3] R. Lenzen, R. Hofmann, P. Bizenberger, A. Tusche, *Astronomical Telescopes & Instrumentation* **1998**, *3354*, 606.

[4] G. R. Carruthers, T. Page, *Science* **1972**, *177*, 788.

[5] T. Chen, P. B. Catrysse, A. El Gamal, B. A. Wandell, *Electron. Imaging* **2000**, *3965*, 451.

[6] J. Farrell, F. Xiao, S. Kavusi, *Electron. Imaging* **2006**, *6069*, 60690N.

[7] A. Tournier, F. Leverd, L. Favennec, C. Perrot, L. Pinzelli, M. Gatefait, N. Cherault, D. Jeanjean, J. Carrere, F. Hirigoyen *et al.*, *IISW* **2011**, *1*, 12.

[8] R. Nixon, N. Doudoumopoulos, E. R. Fossum, *Backside illumination of CMOS image sensor* **2002**, US Patent 6,429,036.

[9] *iPhone 6S And iPhone 6S Plus: Best And Worst Camera Features*, `http://www.forbes.com/sites/paulmonckton/2015/09/12/`

`iphone-6s-and-iphone-6s-plus-camera-features/#889ed427805c`, **2015**, [Online; accessed 15-01-2017].

[10] D. J. Guerrero, W. DiMenna, T. D. Flaim, R. Mercado, S. Sun, *Electron. Imaging* **2003**, *5017*, 298.

[11] R. Rajasekharan, E. Balaur, A. Minovich, S. Collins, T. D. James, A. Djalalian-Assl, K. Ganesan, S. Tomljenovic-Hanic, S. Kandasamy, E. Skafidas *et al.*, *Sci. Rep.* **2014**, *4*, 6435.

[12] D. Fleischman, L. A. Sweatlock, H. Murakami, H. Atwater, *Opt. Express* **2017**, *25*, 27386.

[13] T. D. James, P. Mulvaney, A. Roberts, *Nano Lett.* **2016**, *6*, 3817.

[14] X. Zhu, C. Vannahme, E. Højlund-Nielsen, N. A. Mortensen, A. Kristensen, *Nat. Nanotechnol.* **2016**, *11*, 325.

[15] A. Kristensen, J. K. Yang, S. I. Bozhevolnyi, S. Link, P. Nordlander, N. J. Halas, N. A. Mortensen, *Nat. Rev. Mater.* **2017**, *2*, 16088.

[16] X. M. Goh, Y. Zheng, S. J. Tan, L. Zhang, K. Kumar, C.-W. Qiu, J. K. Yang, *Nat. Commun.* **2014**, *5*, 5361.

[17] N. Liu, M. Mesch, T. Weiss, M. Hentschel, H. Giessen, *Nano Lett.* **2010**, *10*, 2342.

[18] S. U. Lee, B.-K. Ju, *Sci. Rep.* **2017**, *7*, 40649.

[19] V. Vashistha, G. Vaidya, R. S. Hegde, A. E. Serebryannikov, N. Bonod, M. Krawczyk, *ACS Photonics* **2017**, *4*, 1076.

[20] C. Williams, G. Rughoobur, A. J. Flewitt, T. D. Wilkinson, *Sci. Rep.* **2017**, *7*, 7745.

[21] S. Yokogawa, S. P. Burgos, H. A. Atwater, *Nano Lett.* **2012**, *12*, 4349.

[22] D. Baierl, L. Pancheri, M. Schmidt, D. Stoppa, G.-F. Dalla Betta, G. Scarpa, P. Lugli, *Nat. Commun.* **2012**, *3*, 1175.

[23] C. Biswas, Y. Kim, Y. H. Lee, *Sci. Rep.* **2016**, *6*, 37857.

[24] E. Panchenko, J. J. Cadusch, T. D. James, A. Roberts, *ACS Photonics* **2016**, *3*, 1833.

[25] E. Panchenko, J. J. Cadusch, O. Avayu, T. Ellenbogen, T. D. James, D. Gómez, A. Roberts, *Adv. Mater. Technol.* **2018**, *3*, 1700196.

[26] B. Luk'yanchuk, N. I. Zheludev, S. A. Maier, N. J. Halas, P. Nordlander, H. Giessen, C. T. Chong, *Nat. Mater.* **2010**, *9*, 707.

[27] H. Zimmermann, *Integrated Silicon Optoelectronics*, Springer **2010**.

[28] D. Allan, P. Smith, J. Bowie, *Vacuum* **1985**, *35*, 543.

[29] J. Yu, C.-X. Shan, Q. Qiao, X.-H. Xie, S.-P. Wang, Z.-Z. Zhang, D.-Z. Shen, *Sensors* **2012**, *12*, 1280.

[30] P. Irvin, Y. Ma, D. F. Bogorin, C. Cen, C. W. Bark, C. M. Folkman, C.-B. Eom, J. Levy, *Nat. Photonics* **2010**, *4*, 849.

[31] E. Palik, *Handbook of Optical Constants of Solids*, Academic Press **1998**.